

Journal of Biomedical Optics

SPIDigitalLibrary.org/jbo

Single-beam, dual-view digital holographic interferometry for biomechanical strain measurements of biological objects

Dejan V. Pantelić
Dušan Ž. Grujić
Darko M. Vasiljević

Single-beam, dual-view digital holographic interferometry for biomechanical strain measurements of biological objects

Dejan V. Pantelić,* Dušan Ž. Grujić, and Darko M. Vasiljević

University of Belgrade, Institute of Physics, Pregrevica 118, Zemun 11080, Belgrade, Serbia

Abstract. We describe a method for dual-view biomechanical strain measurements of highly asymmetrical biological objects, like teeth or bones. By using a spherical mirror, we were able to simultaneously record a digital hologram of the object itself and the mirror image of its (otherwise invisible) rear side. A single laser beam was sufficient to illuminate both sides of the object, and to provide a reference beam. As a result, the system was mechanically very stable, enabling long exposure times (up to 2 min) without the need for vibration isolation. The setup is simple to construct and adjust, and can be used to interferometrically observe any object that is smaller than the mirror diameter. Parallel data processing on a CUDA-enabled (compute unified device architecture) graphics card was used to reconstruct digital holograms and to further correct image distortion. We used the setup to measure the deformation of a tooth due to mastication forces. The finite-element method was used to compare experimental results and theoretical predictions. © 2014 Society of Photo-Optical Instrumentation Engineers (SPIE) [DOI: [10.1117/1.JBO.19.12.127005](https://doi.org/10.1117/1.JBO.19.12.127005)]

Keywords: digital holography; interferometry; aberration correction; finite element method; dentistry.

Paper 140481R received Aug. 27, 2014; accepted for publication Nov. 10, 2014; published online Dec. 17, 2014.

1 Introduction

It is commonly perceived that a hologram records the full, three-dimensional (3-D) image of an object. In reality, the size and the position of the holographic plate relative to the object determine the content of the hologram. In this sense, a hologram is a fixed “window” onto the virtual, 3-D world. The holographic plate is an aperture through which to observe an object from a limited angular range perspective, without the possibility of “walking around” the hologram to observe its more distant side. The problem is even more pronounced in digital holography, which is limited by the small dimensions of CCD/CMOS chips (compared to classical holographic plates) and an inability to display a true 3-D image on the computer monitor.

The ability to see an object (especially a very asymmetrical one) from all directions can be important for some applications. Holographers have tried to record “walk-around” holograms, particularly for display holography. That involved bending the holographic film so as to surround the object, thereby widening the observation “window”. Cylindrical^{1,2} (e.g., Cross Lloyd’s famous “kiss” hologram³), conical,⁴ alcove,⁵ and disk-type⁶ holograms are well known in this context.

The problem of observation from multiple-viewpoints was also tackled by other means, usually involving a finite number of viewpoints. One approach uses additional computer processing in digital holography.⁷ Another approach uses several observation angles with appropriate processing for use in a digital holographic microscopy⁸ or holographic particle image velocimetry.⁹

The problem of viewing an object from several perspectives also exists in holographic interferometry. Unfortunately, the above approaches are not readily applicable and other techniques have been used so far. Transparent objects have been successfully

analyzed using scatter plates or by probing with several beams.¹⁰ A dual-channel holographic interferometer, with holographic optical elements, was proposed for the study of phase objects.¹¹ Opaque objects have been surrounded by flat mirrors to achieve separate views.¹² However, the typical distances between the images and the object in such arrangements are problematic for digital holography because of the spatial-frequency limitation of the charge-coupled device (CCD) detectors.

Full-view observations are also problematic in the field of biomechanics, where objects of interest are often very asymmetrical. Numerous techniques have been used such as moiré,¹³ speckle interferometry,¹⁴ and holography.¹⁵ Usually, they reveal surface deformations while internal stresses remain hidden and require mathematical modeling using the finite-element method (FEM). Holography has been extensively used to observe minute tissue deformations under mechanical stress.^{16,17} We previously described a dual-beam off-axis holographic interferometry method that used a single spherical mirror to simultaneously observe the front and rear of a tooth model.¹⁸ The mirror produced a real, strongly distorted, image of the object placed at the center of curvature.

Here, we present a digital holographic method that uses a spherical mirror and a single expanded laser beam to observe and to illuminate an object from both sides while also generating the reference beam. The setup has excellent mechanical stability, because all the necessary beams are generated from the same input beam as in the local-reference beam configuration.¹⁹ Our proposed technique can also be regarded as an extension and improvement of single-beam holography,²⁰ one of the simplest holographic methods. The digital nature of the method enables correction of image distortion and avoids wet chemistry. The

*Address all correspondence to: Dejan V. Pantelić, E-mail: pantelic@ipb.ac.rs

technique is generally applicable and can be used for holographic interferometry on any object of dimensions that are limited by the diameter of the spherical mirror.

To demonstrate the capabilities of the proposed technique, we present an interferometric measurement of tooth deformation resulting from mastication. A tooth is inherently asymmetrical, and we reveal the deformation-field asymmetry in the holographically generated interference images. We used a digital tooth model and the FEM to calculate the resulting deformation and for comparison with experiments.

2 Experimental Technique

The paraxial image of an object placed in front of a concave spherical mirror is formed according to a well-known spherical mirror equation. In particular, if the object is positioned at the center of curvature the image appears at the same distance from the mirror. The image is inverted, real, and has unit magnification. This configuration was used throughout our experiments.

As an illustration, Fig. 1(a) shows several rays incident on a tilted concave spherical mirror (M). An arbitrary object (O) is positioned at the center of curvature (R). Rays 3 to 6 clearly illuminate the front surface of the object and the scattered radiation can be directly captured by an observer (or detector S). Some of

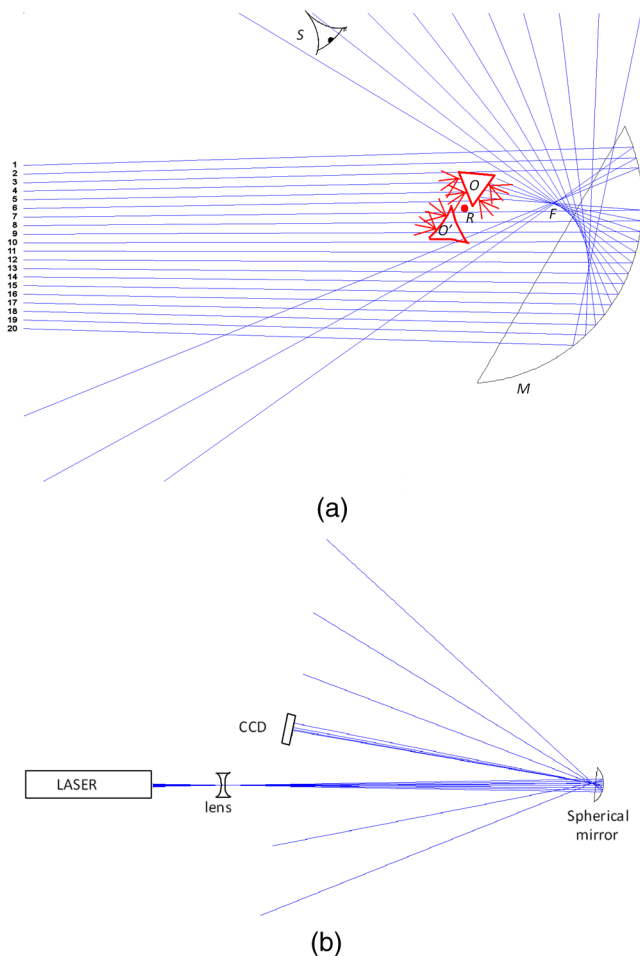


Fig. 1 (a) An object (O) is placed at a distance $2f$ from the spherical mirror (M) (f – focal distance) and its image is formed at O' . R is the center of curvature, F is the focal point of the beams reflected from the mirror, and S is observation (detection) direction; (b) the experimental setup.

the rays (7 to 10) that miss the object and are reflected from the mirror illuminate the object from the rear. The scattered radiation is again reflected by the mirror, and produces an image (O') of the back side of the object. The rays that miss both the front and the rear side (i.e., 1, 2, and 11 to 20) continue to propagate, and are used as a reference beam in a holographic experiment.

In our experiment, we used a CW diode-pumped Nd-YAG laser operating at the second harmonic (532 nm wavelength, 100 mW power) to illuminate the object. The coherence length of the laser was 100 m, but a short-coherence laser (e.g., He-Ne) can also be used, because the path length difference between the object and the reference beams is of the order of several centimeters. The laser beam was expanded by a diverging lens and used to fill the aperture of the spherical mirror (aperture diameter 75.3 mm, radius of curvature 46 mm, and focal length 23 mm). Mirror quality is not very important; in fact, we used a mirror from an old projection device. The short focal distance strongly distorts the mirror image, as seen in the photograph (Fig. 2). For small objects (of the order of 1 cm), the distortion is weak and the setup is adequate. Larger objects require computer-based compensation of the aberration to yield meaningful measurements. This procedure will be described in detail in the next section.

A digital single-lens reflex camera (Canon EOS50d, with an APS-C CMOS sensor with 14-bit dynamic range, 25.1×16.7 mm dimensions, and a 4752×3168 image size) recorded

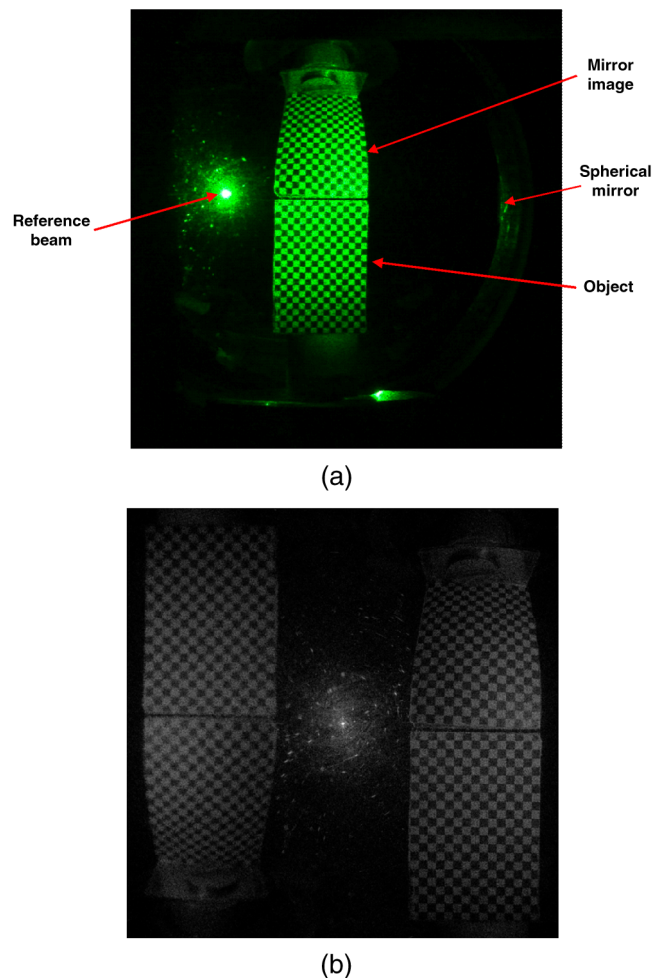


Fig. 2 (a) Photograph of a test object: a flat plate, checked on both sides (down), its mirror image (up), and the reference beam (left). (b) Holographic reconstruction of the test object.

the holograms, in either RAW or JPG format, before further processing by computer. The setup is schematically presented in Fig. 1(b).

The object is positioned as previously described [Fig. 1(a)], but with a slight displacement from the optical axis to avoid blocking its own image (i.e., O and O' do not overlap). Finally, an observer simultaneously sees the object O , its mirror image O' , and a reference beam, produced by the laser beam being focused by the mirror [see photograph in Fig. 2(a)].

Several other factors must be taken into account when generating the hologram. The most important is the distance between the object and the CCD camera, which should be such that the spatial frequencies of the hologram can be resolved by the CCD chip (e.g., a $4.7\text{-}\mu\text{m}$ inter-pixel distance for an EOS 50d camera). In our setup, the distance must be larger than approximately 0.7 m. Another issue is the reference-to-object beam ratio for achieving a deep modulation of the holographic interference pattern. In our experience, this is not critical as the dynamic range of a detector is high (14 bit). If necessary, we placed an additional neutral density filter in the reference beam to better adjust the reference-to-object beam intensity ratio. Most of the time, we used the setup without additional optical components.

The final holograms, having 4752×3168 pixels, were transferred to a computer and numerically processed on a CUDA-enabled graphics card (NVidia GeForce 560Ti) using a computational wave optics (CWO) software package²¹ (under the computer physics communications program library CPC nonprofit use license agreement,²² for parallel processing. A holographic reconstruction of the test object in Fig. 2(a) is shown in Fig. 2(b). The zeroth diffraction order is in the middle and the useful orders are visible on the left and right. A shifted Fresnel algorithm²³ was mainly used, allowing the efficient separation of the useful diffraction order from the other two. This kind of algorithm enables shifting of the reconstruction window with respect to the hologram, while the window size can be arbitrarily chosen. The algorithm is applicable to long propagation distances. For distortion correction, in addition to the shifted Fresnel algorithm, we had to use the convolution-type (angular frequency²¹) algorithm, which is valid for short propagation distances.

3 Computational Correction of the Image Distortion

Aberration correction is most usually directly performed in an optical system using additional optical components, and making it complicated and costly. On the other hand, digital holography is an ideal ground for digital aberration correction, since both the phase and the amplitude of the optical field are known.²⁴ In our case, the image is sharp, but distorted. We solved the problem by digitally backpropagating the image through the spherical mirror all the way to the object location.

The simplified geometry of the spherical mirror imaging system is shown in Fig. 3. As explained above, spherical mirror M produces an image I_B of the object backside O_B [Fig. 3(a)]. The hologram was recorded and reconstructed to simultaneously reveal the image of the front (O_F) and the distorted image (I_B) of the back. The distortion of image I_B was corrected by reversing the propagation direction of the corresponding wave field and reflecting it off the mirror [Fig. 3(b)].

The exact calculation of the distortion compensation is more complicated than it seems. This is a consequence of the variable

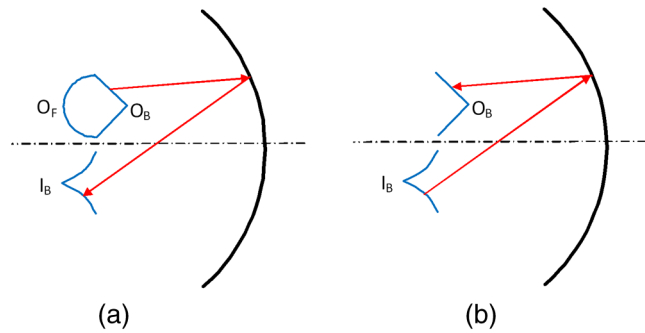


Fig. 3 (a) The backside (O_B) of an object produces a distorted image (I_B) after reflecting from the spherical mirror. (b) The aberration is software-compensated by backpropagating the reconstructed wavefront.

magnifications across the field of an imaging system.²⁵ To demonstrate this in our particular case, we consider an annular section of the mirror, as shown in Fig. 4. A light field propagates and reflects from the annulus. The process is mathematically described as a multiplication of the field with a corresponding phase factor. Generally speaking, the phase factor is complicated²⁶ but can be approximated to a spherical wavefront. Within this approximation, the annulus focuses the wavefront to the point F in Fig. 4. Considering the annulus as a simple spherical mirror with radius of curvature R , it follows that its focal distance f (equal to the radius of the reflected spherical wavefront) varies with height h as

$$f = \sqrt{R^2 - h^2} - \frac{R^2}{2\sqrt{R^2 - h^2}}. \quad (1)$$

Thus, the required phase factor is a spherical wavefront with radius f .

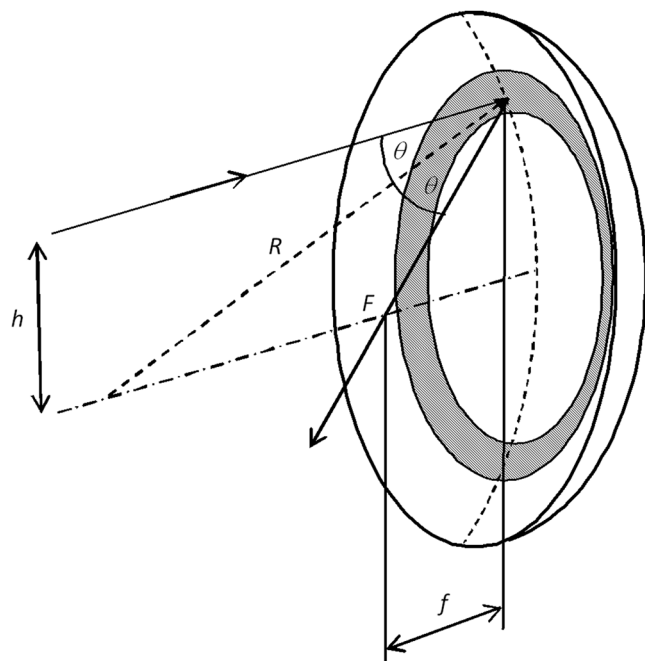


Fig. 4 The focal length f of an annular section of the mirror depends on the height h and the mirror radius of curvature R .

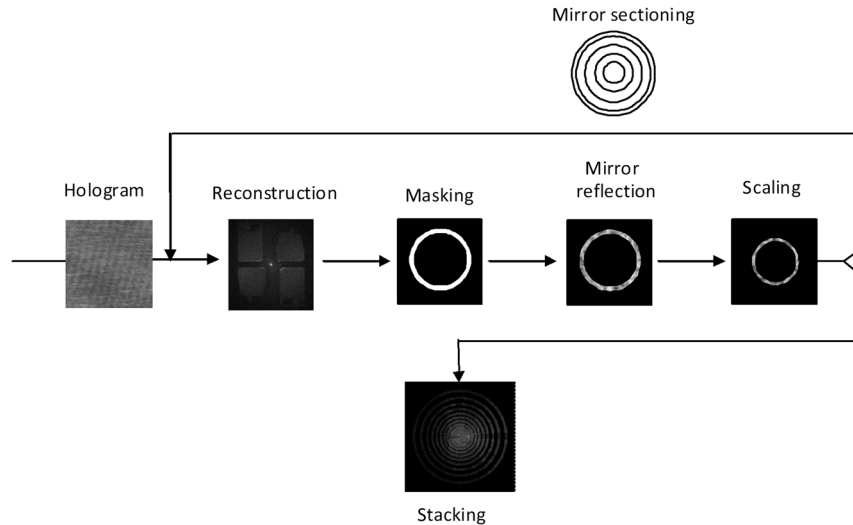


Fig. 5 Schematic of the distortion-correction procedure. A mirror is divided into annular sections, and the wavefront is backpropagated through each section.

To solve the complete problem, a given mirror is divided into a set of annular sections and the problem is analyzed section by section. The hologram is reconstructed and a wavefront propagates to each section. The field is masked by the corresponding annular aperture and is multiplied by the appropriate spherical phase factor before propagating back to the image plane. The whole procedure is summarized in Fig. 5, and mathematical details are given in the Appendix.

We verified the method by using the test object shown in Fig. 2: a plate, checkered on both sides with 1 mm squares. A hologram was recorded as described in Sec. 2, and a single-diffraction order was extracted [Fig. 6(a)], where the object and its (distorted) mirror image are seen one above the other. The image resulting from the distortion correction is shown in the upper part of Fig. 6(b). The final result is a set of two images that contain the complete dual-view information on the object [red squares in Figs. 6(a) and 6(b)].

It is important to note that the complete phase information is preserved during distortion correction. This means that distortion correction can be applied to holographic interferograms. To verify this possibility, we used another test object [a rectangular aluminum block with a blind hole—Fig. 7(a)] that could be mechanically loaded using a brass tool with a spherical tip (sphere diameter 5.5 mm). Two holograms were recorded for the unloaded and loaded objects. The resulting interferogram is shown in Fig. 7(b). Its distortion-corrected version is shown in Fig. 7(c).

The distortion-correction process is notably time consuming, as the Fresnel transform must be performed several times. A high-quality reconstruction requires the reconstructed image to be divided into 40 to 80 circular sections (as described in Sec. 3). The Fresnel transform must be performed twice for each section: the first transform is of the “shifted Fresnel” type,²³ and the second transform is of the “angular spectrum” type.²¹ We used parallel computing on a graphics card, and the image reconstruction from a hologram (2048 × 2048 pixels) lasts 2.5 s, without distortion correction. The correction process is more time consuming and lasts up to 2 min, depending on the number of sections used through the process.

4 Finite-Element Modeling of Dental Tissue

Our aim was to use the holographic technique (described in Secs. 2 and 3) to measure deformations in dental tissue due to mastication forces. In order to calculate internal stresses, we had to develop a realistic FEM model of a tooth.

We used a human upper second premolar that had been extracted for orthodontic reasons. The tooth was scanned using

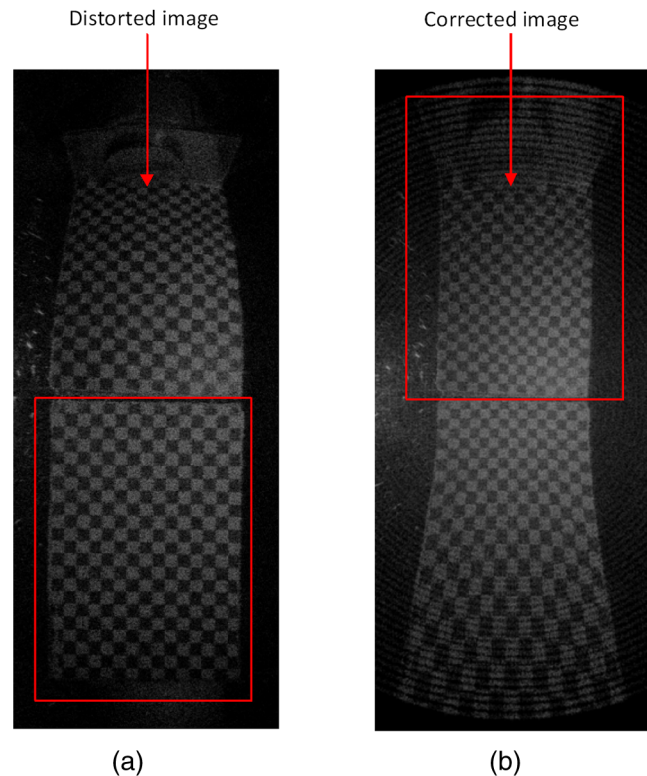


Fig. 6 (a) Single-diffraction order of a reconstructed digital hologram, containing an object (bottom) and its spherical mirror image (top). (b) Distortion-corrected diffraction order. The red squares contain the complete dual-view information about the object.

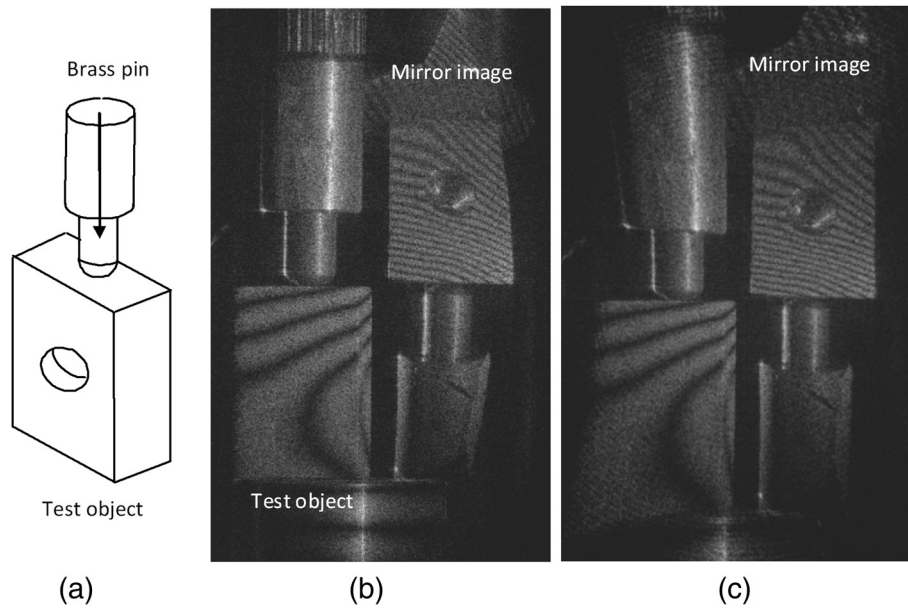


Fig. 7 (a) Diagram of a test object (aluminum block with a blind hole) and a brass loading tool, (b) digital holographic interferogram of the test object, (c) distortion-corrected interferogram. Due to high dynamic range of the resulting image, the intensity scale is logarithmic.

a 64-slice CT scanner (Sensation 64 Cardiac CT, manufactured by Siemens, Germany). Forty-two slices were sufficient to acquire the whole tooth with a 0.5 mm resolution between consecutive slices. Within each slice, we were able to resolve 110×88 pixels with a 0.1 mm resolution.

This set of slice images was the starting point for creating a 3-D solid model. All images were segmented by applying an intensity threshold to identify the boundaries among the enamel, dentin, and pulp regions. One of the slices and its corresponding segmented image are given in Figs. 8(a) and 8(b), respectively. The result was saved as a series of data files in drawing exchange format in order to facilitate importing into a 3-D solid modeling program.

The 3-D solid model was constructed by first defining contours using splines, and then building the 3-D solid body from the set of splines. The procedure was repeated for each tooth structure: the enamel, the dentin, and the pulp. The resulting 3-D solid model of the whole human maxillary premolar is displayed in Fig. 9.

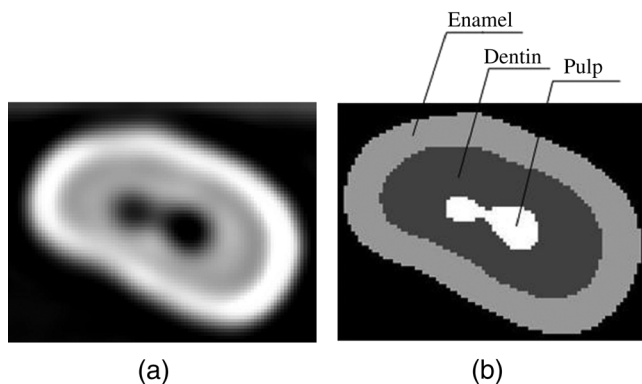


Fig. 8 (a) One CT slice of a human upper second premolar tooth. (b) The corresponding segmented image.

In order to calculate the various types of stress and strain using the FEM, the fixture, the load, and the mesh had to be defined. The exterior nodes on the dentin surface were fixed in all directions and could neither translate nor rotate. A load was applied at the two points on the cusps indicated by green arrows in Fig. 9(b). Parabolic tetrahedral solid elements (defined by four corner nodes, six mid-side nodes, and six edges) were used for meshing, as they more accurately represent

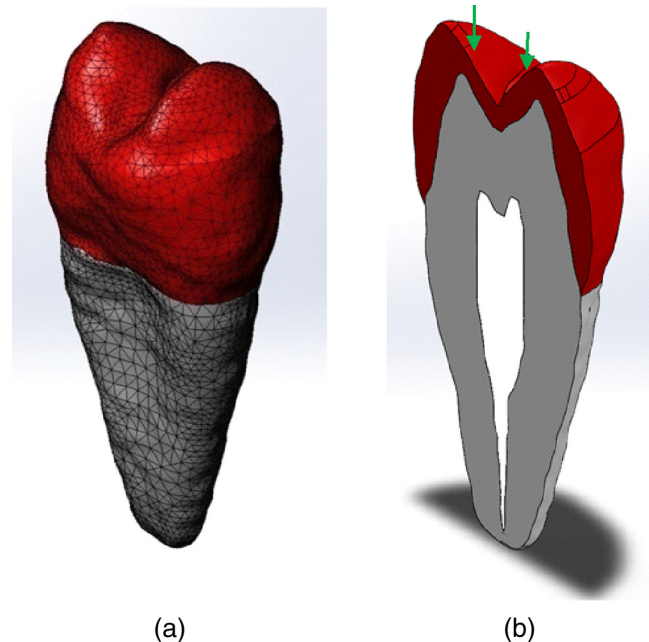


Fig. 9 Three-dimensional (3-D) solid model of a human maxillary premolar: (a) a meshed model and (b) its cross section (red—enamel, gray—dentine, white—pulp, green arrows indicate application points mechanical forces).

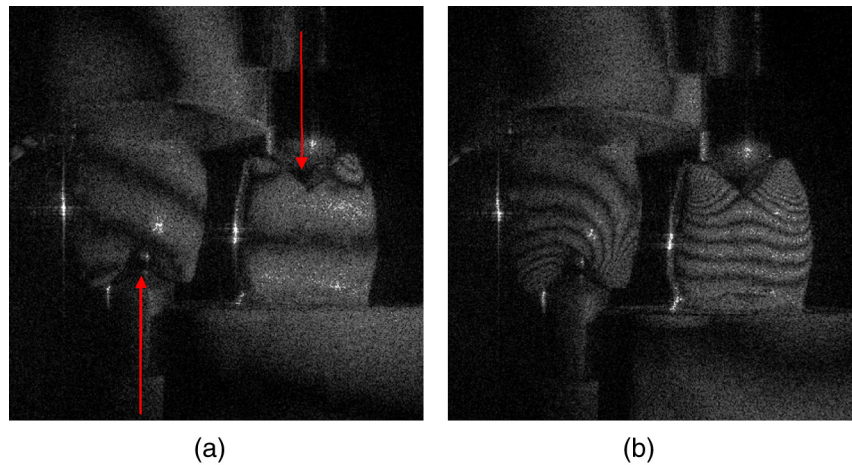


Fig. 10 Interferograms of an artificial tooth under (a) 100 N and (b) 250 N loads applied by a brass tool. The red arrows indicate the load directions. Due to high dynamic range of the resulting image, the intensity scale is logarithmic.

curved boundaries. The final 3-D model had 174,196 nodes and 118,126 elements.

5 Dual-View Measurement of Masticatory Effects Using Holographic Interferometry

We analyzed a problem of stress and strain acting on a single tooth during mastication. The results, obtained by dual-view holographic interferometry (as described in Secs. 2 and 3), were compared with the FEM (see Sec. 4).

Experiments were performed using a physical model of a tooth obtained by rapid prototyping (one possible method for fabricating a substitute for a human tooth in dental research).²⁷ The digital 3-D model was used as the input for a 3-D printer to generate a plastic copy of a real tooth. The mechanical properties of the resulting model certainly do not match those of the original (the elastic modulus of dentin is 7 to 46 GPa, that of enamel 80 to 1800 GPa,²⁸ compared with 2.5 GPa for the plastic model), but can be used to assess correspondences between the numerical FEM model and experimental results. An additional advantage is the availability of many samples with no medical or ethical implications.

The tooth model was mounted in a hollow aluminum cylinder and permanently fixed with dental gypsum. The root was completely embedded in the gypsum, while the entire tooth crown was visible and accessible to holographic measurements. A brass tool with a spherical head (shown schematically in Fig. 7(a), similar to that in Ref. 29) was used to controllably apply force to the tooth. The force was directed along the long tooth axis (red arrow in Fig. 10) and its magnitude was measured with a force gauge. The tooth was positioned in front of a spherical mirror, as previously described. A reference hologram was recorded with no force applied. As the force was then varied between 20 and 250 N, corresponding holograms were recorded, and interferograms were calculated (two examples shown in Fig. 10). We would like to note that the phase difference information could be useful in some instances, such as contouring. In our case, classical interferograms were enough to test the correspondence between the experiment and FEM modeling.

From the computational point of view, the digital tooth model has uniform mechanical properties [as shown in Fig. 11(a)], corresponding to the physical model manufactured

by 3-D printing. The loading configuration is shown in Fig. 11(b), where the tool orthogonally acts to tooth cusps, imitating the experimental configuration. The force was varied within the experimental range (20 to 250 N). The computational results are shown in Figs. 12(a) and 12(b), where the deformation on both sides of a tooth can be seen, encoded by pseudo-colors. It is not possible to completely replicate the intricate shape of a tooth and determine the position of contact points between the tooth and the pressing tool, as well as the direction of the force. Taking all that into account, FEM modeling reproduces reasonable experimental results.

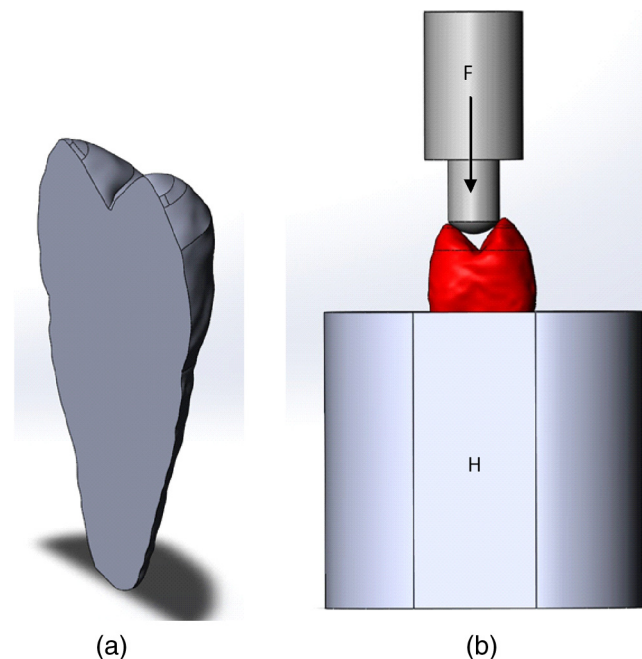


Fig. 11 (a) Cross section of a finite-element model (FEM) with uniform mechanical properties corresponding to a physical tooth model manufactured by rapid prototyping. (b) A tooth model mounted in a holder (H), with a spherical-tip loading tool (F is an externally applied force).

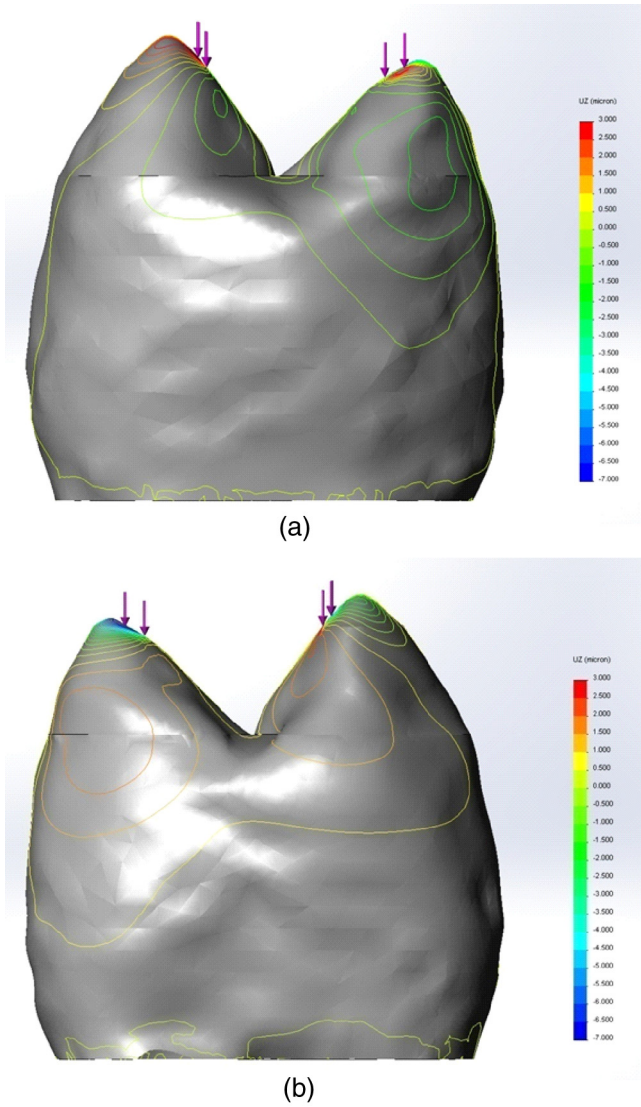


Fig. 12 Simulated deformation of an artificial tooth, calculated using FEM: (a) front side, (b) back side.

6 Discussion and Conclusions

The technique described in this study is universally applicable, but several points should be taken into account. First, we found that the method can be used without aberration correction if the object is smaller than approximately one-third of the mirror aperture. Under this condition, distortion is negligible and no corrections are needed. The image of larger objects becomes strongly distorted near the edge of the aperture (see Fig. 2) and requires numerical compensation as previously described. By using larger mirrors (of 15 to 20 cm diameter), objects with a size of the order of 5 cm could be investigated.

The mechanical stability of the whole system is excellent, since the reference and object beams are generated from the same illuminating beam. Therefore, moving the illuminating beam similarly affects both the reference and object beams. Consequently, the interference pattern is negligibly perturbed provided the beam deviation is not too large. In practice, holograms were recorded on an optical table without any vibration isolation and the camera was mounted on a tripod placed on the ground (away from the table); yet, the holograms produced were of excellent quality. To directly test the stability more, we deliberately reduced the laser beam

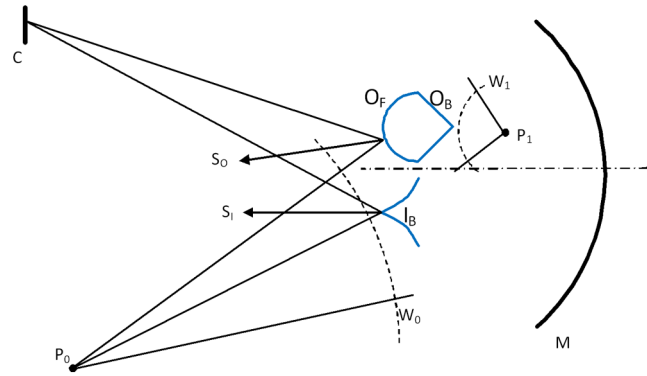


Fig. 13 Sensitivity vectors S_0 and S_1 of an object and its mirror image, respectively. M is the spherical mirror, P_0 an illumination source, W_0 the corresponding wavefront, P_1 the conjugate mirror image of P_0 , and W_1 the corresponding wavefront. O_F and O_B are the front and back sides of the object, respectively, and I_B is the mirror image of the back side O_B . C is the camera detector.

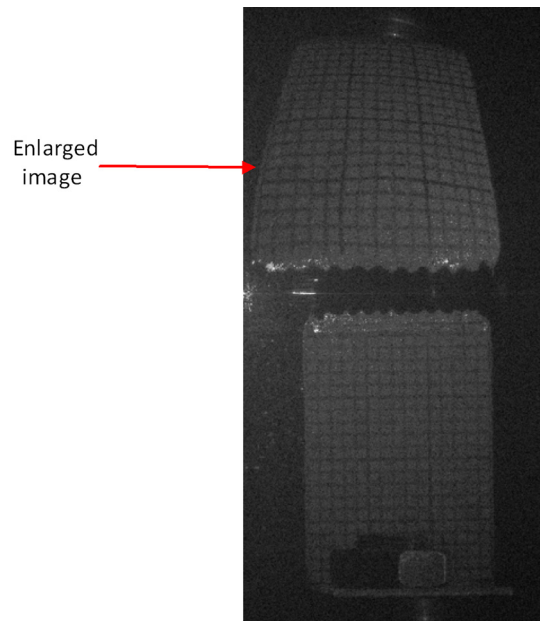


Fig. 14 Enlarged back side of an object.

intensity in order to increase the exposure. We were able to record high-quality holograms even for an exposure time of 2 min.

Interpreting fringes requires an estimation of the sensitivity vector.³⁰ This is simple in the case of the object itself (its front side O_F in Fig. 13), because the sensitivity vector (S_0) simply bisects the angle between the illumination and observation directions. This vector is fairly constant since the object is small, the curvature radius of the object beam is large, and the observation direction is fixed by the position of the camera chip (C). The situation is more complicated with the mirror image I_B and its associated sensitivity vector. First, we have to note that the back-side O_B is illuminated with the wavefront W_1 . It is generated by the point source P_1 , which is conjugate to the illuminating source P_0 . The conjugate mirror images of O_B , W_1 , and P_1 are I_B , W_0 , and P_0 , respectively, and this is what we observe in reality. We conclude that the sensitivity vector S_1 of the mirror image is defined by the illumination direction $P_0 I_B$ and the observation direction $C I_B$. Again, the sensitivity vector S_1 is constant, for the same reasons as for vector S_0 .

An additional benefit of the method is the possibility to enlarge the image by simply moving the object closer to the mirror. Even though the distortion will be larger, it can be corrected by the algorithm described in Sec. 3. This allows more details to be observed, albeit on only one object surface (Fig. 14).

There are also small experimental issues. The illumination level of the object and its image should be approximately the same. By properly aligning and positioning the Gaussian illuminating beam, we achieved a sufficiently even illumination. If necessary, the part of the beam that illuminates the front can be easily filtered with a neutral density filter. It is required to mask stray radiation, as in almost any holographic setup. If more than two separate views are needed, additional spherical mirrors can be used.

In conclusion, we have simultaneously described a simple technique for observing the front and back sides of an object by holographic interferometry. Only one spherical mirror and a single laser beam are needed to illuminate the object from both sides and to produce a reference beam. The setup is mechanically very stable because it resembles that used in local reference beam techniques. The proposed method is versatile and can be adapted to many experimental situations, providing that the object is smaller than the mirror. We illustrated the benefits of the proposed scheme by performing holographic interferometry of the dental model manufactured by rapid prototyping.

Appendix: Mathematical Procedure and Algorithm for Distortion Correction

The principle of aberration correction is explained in Sec. 3 and schematically presented in Fig. 5. The mathematics discussed in this Appendix refers to Fig. 15.

For simplicity, all the following equations are one-dimensional, but can be straightforwardly rewritten in the proper

two-dimensional form. Our calculations use a Fresnel integral defined as

$$U(x_2) = \frac{\exp\left(i\frac{2\pi}{\lambda z}\right)}{i\lambda z} \exp\left(i\frac{\pi}{\lambda z}x_2^2\right) \int_{-\infty}^{\infty} u(x_1) \times \exp\left(i\frac{\pi}{\lambda z}x_1^2\right) \exp\left(-i\frac{2\pi}{\lambda z}x_1x_2\right) dx_1. \quad (2)$$

Propagation (distance z) from the hologram plane to the plane of the mirror section S_j is approximated by the following Fresnel integral (as the propagation distance is largely compared to the hologram dimensions)

$$u_0(x_z) = \exp\left(\frac{i\pi}{\lambda z}x_z^2\right) \int_{-\infty}^{\infty} u(x) \exp\left(\frac{i\pi}{\lambda z}x^2\right) \exp\left(-i\frac{2\pi}{\lambda z}x_zx\right) dx. \quad (3)$$

This equation can be described as the product

$$u_0(x_z) = \exp\left(i\frac{\pi}{\lambda z}x_z^2\right) P(x_z), \quad (4)$$

of a quadratic (oscillatory) phase factor and an integral expression

$$P(x_z) = \int_{-\infty}^{\infty} u(x) \exp\left(i\frac{\pi}{\lambda z}x^2\right) \exp\left(-i\frac{2\pi}{\lambda z}x_zx\right) dx. \quad (5)$$

The resulting equation accurately describes the resulting field, except for the fact that the quadratic phase factor quickly oscillates and is aliased during computation (because of finite sampling). Therefore, the field distribution defined by u_0 [Eq. (4)] cannot be numerically propagated further without introducing

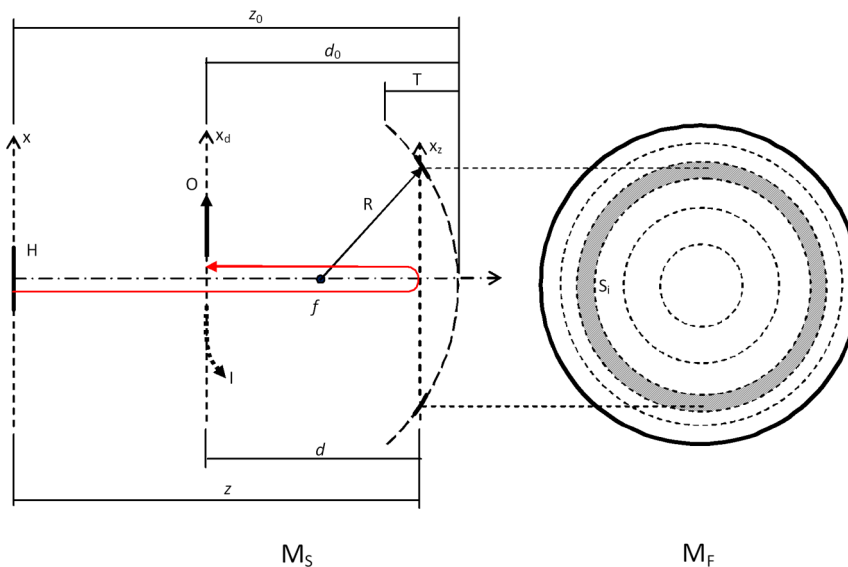


Fig. 15 Two orthogonal views (side view is on the left and front view is on the right) of the spherical mirror divided into a set of annular sections. H —a hologram (CCD chip), I —aberrated image, O —corrected image, R —mirror radius, x , x_d , and x_z are the hologram-plane, image-plane, and intermediate-plane locations, respectively. M_S —side view of the mirror, M_F —front view of a mirror, divided into a set of sections S_j . Symbols z , d , T , z_0 , d_0 and are the geometrical dimensions and the propagation distances used in the calculations. The red arrow shows the order of wavefront calculations, starting from the hologram plane x , propagating to the intermediate plane x_z (containing the section S_j), and then backpropagating to the image plane x_d .

artifacts.³¹ However, the integral itself [Eq. (5)] does not oscillate.

The wave is further reflected from the mirror and the field distribution, defined by Eq. (4), must be multiplied by the corresponding spherical phase factor

$$u_1(x_z) = \exp\left(i\frac{\pi}{\lambda f}x_z^2\right)u_0(x_z), \quad (6)$$

where f is the focal length of the mirror section. The reflected field, Eq. (6), further propagates a distance d to the image plane, and is then described by

$$u_2(x_d) = \exp\left(i\frac{\pi}{\lambda d}x_d^2\right)\int_{-\infty}^{\infty}u_1(x_z)\exp\left(i\frac{\pi}{\lambda d}x_z^2\right)\times\exp\left(-i\frac{2\pi}{\lambda d}x_dx_z\right)dx_z. \quad (7)$$

By substituting u_1 [Eq. (6)] into Eq. (7) and using the relation between u_0 and $P(x_z)$ [Eq. (4)], we get

$$u_2(x_d) = \exp\left(i\frac{\pi}{\lambda d}x_d^2\right)\int_{-\infty}^{\infty}P(x_z)\exp\left(i\frac{\pi}{\lambda z}x_z^2\right)\times\exp\left(i\frac{\pi}{\lambda f}x_z^2\right)\exp\left(i\frac{\pi}{\lambda d}x_z^2\right)\exp\left(-i\frac{2\pi}{\lambda z}x_dx_z\right)dx_z. \quad (8)$$

We define an equivalent propagation distance z_e with

$$\frac{1}{z_e} = \frac{1}{d} + \frac{1}{f} + \frac{1}{z}. \quad (9)$$

The diffraction integral [Eq. (8)] is then written more compactly as

$$u_2(x_d) = \exp\left(i\frac{\pi}{\lambda d}x_d^2\right)\int_{-\infty}^{\infty}P(x_z)\exp\left(i\frac{\pi}{\lambda z_e}x_z^2\right)\times\exp\left(-i\frac{2\pi}{\lambda d}x_dx_z\right)dx_z. \quad (10)$$

Observe that the final integral is slightly different from the standard Fourier form of the Fresnel diffraction integral (1). The difference is in the exponential terms in the integrand, which should have the same constant factor $\pi/\lambda z$. To reduce the integral in Eq. (8) into a standard form [as in Eq. (2)], we scale the variable x_d as

$$x_d = \frac{z_e}{d}\xi, \quad (11)$$

and finally obtain the integral

$$u_2(\xi) = \exp\left(i\frac{\pi z_e^2}{\lambda d^3}\xi^2\right)\int_{-\infty}^{\infty}P(x_z)\exp\left(i\frac{\pi}{\lambda z_e}x_z^2\right)\times\exp\left(-i\frac{2\pi}{\lambda z_e}\xi x_z\right)dx_z. \quad (12)$$

By separating the quadratic phase factor and the integral, we get

$$u_2(\xi) = \exp\left(i\frac{\pi z_e^2}{\lambda d^3}\xi^2\right)P_1(\xi), \quad (13)$$

where

$$P_1(\xi) = \int_{-\infty}^{\infty}P(x_z)\exp\left(i\frac{\pi}{\lambda z_e}x_z^2\right)\exp\left(-i\frac{2\pi}{\lambda z_e}\xi x_z\right)dx_z. \quad (14)$$

The result of the above integral must be scaled from ξ back to the physical coordinates x_d using Eq. (11). During the calculations only the integrals need to be calculated [P in Eq. (5) and P_1 in Eq. (14)]; the quadratic phase factor in Eq. (13) may be subsequently included if necessary.

From the numerical point of view, we started the process by calculating the integral in Eq. (5). In effect, we reconstructed the hologram at a distance z , but omitted the quadratic phase factor. The propagation distance was large and a Fourier form of the Fresnel transform algorithm was used.²¹ The resulting far-field was masked with an annular mask, and was further propagated using Eq. (14), which includes three quadratic phase factors (combined into an equivalent propagation distance z_e [Eq. (9)]. In this step, the propagation distance was short and

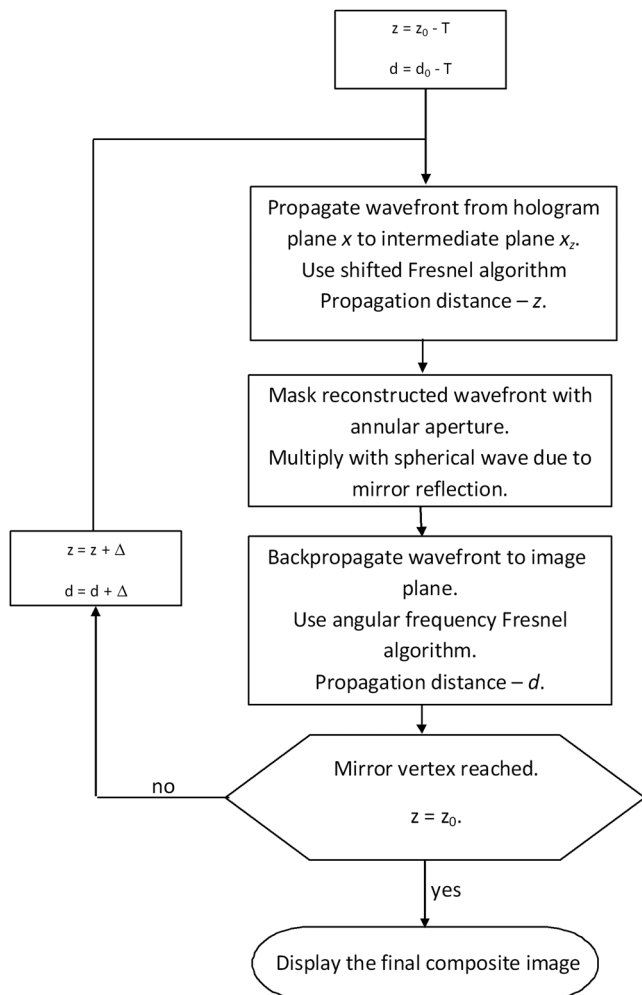


Fig. 16 A flow chart of a distortion-correction algorithm.

a convolution-type (angular frequency²¹) algorithm was used. Finally, the resulting ring-like image was rescaled according to Eq. (11). The whole process was repeated for all the mirror sections, and a set of ring-like images was obtained. These were coherently summed to produce a final distortion-corrected image (with a correction applied to both the phase and amplitude). The whole procedure is visualized in Fig. 5, and the appropriate algorithm flow chart is shown in Fig. 16.

The software was written in C++, based on a previously described algorithm. The CWO library²¹ was used to speed up the computation by using parallel processing on a graphics card.

Acknowledgments

This research was funded by the Serbian Ministry of Education, Science, and Technological Development, under the Contract Nos. ON171038 and III45016. We express our gratitude to Professor Dr. Larisa Blažić, Ivana Kantardžić, and Tatjana Vukadinov, from the University of Novi Sad, Faculty of Medicine, Dental Clinic, Serbia, for helping us with CT scanning of a tooth and three-dimensional (3-D) model construction.

References

1. Y. S. Cheng and R. C. Chang, "Image-plane cylindrical holographic stereogram," *Appl. Opt.* **39**, 4058–4069 (2000).
2. O. D. D. Soares and J. C. A. Fernandes, "Cylindrical hologram of 360° field of view," *Appl. Opt.* **21**, 3194–3196 (1982).
3. S. F. Johnston, *Holographic Visions, a History of New Science*, Oxford University Press, Oxford, United Kingdom (2006).
4. K. Okada et al., "Conical holographic stereograms," *Opt. Commun.* **73**, 347–350 (1989).
5. S. Benton, "Real image holographic stereograms," U.S. Patent No. 4834476 (1989).
6. Y.-S. Cheng, Z.-F. Chen, and C.-H. Chen, "Virtual-image generation in 360 degree viewable image-plane disk-type multiplex holography," *Opt. Express* **21**, 10301–10313 (2013).
7. J. Maycock et al., "Reconstruction of partially occluded objects encoded in three-dimensional scenes by using digital holograms," *Appl. Opt.* **45**, 2975–2985 (2006).
8. Y. Takaki and H. Ohzu, "Hybrid holographic microscopy: visualization of three-dimensional object information by use of viewing angles," *Appl. Opt.* **39**, 5302–5308 (2000).
9. J. Sheng, E. Malkiel, and J. Katz, "Single beam two-views holographic particle image velocimetry," *Appl. Opt.* **42**, 235–250 (2003).
10. R. Jones and C. Wykes, *Holographic and Speckle Interferometry*, Cambridge University Press, Cambridge, United Kingdom (1989).
11. A. K. Sharma et al., "A holographic dual-channel interferometer," *Curr. Sci.* **91**(3), 269–271 (2006).
12. R. K. Erf, "Solid propellant rocket inspection," in *Holographic Nondestructive Testing*, R. K. Erf, Ed., pp. 365–372, Academic Press, New York, London (1974).
13. J. D. Wood et al., "Mapping of tooth deformation caused by moisture change using moiré interferometry," *Dent. Mater.* **19**, 159–166 (2003).
14. L. Yang et al., "Measurement of strain distributions in mouse femora with 3-D-digital speckle pattern interferometry," *Opt. Lasers Eng.* **45**, 843–851 (2007).
15. S. M. Solís, F. M. Santoyo, and M. del Socorro Hernández-Montes, "3-D displacement measurements of the tympanic membrane with digital holographic interferometry," *Opt. Express* **20**, 5613–5621 (2012).

16. G. Caroen et al., "Mastication effort study using photorefractive holographic interferometry technique," *J. Biomech.* **43**, 680–686 (2010).
17. D. Pantelić et al., "Real-time measurement of internal stress of dental tissue using holography," *Opt. Express* **15**, 6823–6830 (2007).
18. D. Pantelić et al., "Holographic measurement of a tooth model and dental composite contraction," *Mater. Manuf. Processes* **24**, 1142–1146 (2009).
19. H. J. Caulfield, "Information retrieval from local reference beam holograms," *Phys. Lett.* **27A**, 319–320 (1968).
20. P. Hariharan, *Basics of Holography*, Cambridge University Press, Cambridge, United Kingdom (2002).
21. T. Shimobaba et al., "Computational wave optics library for C++: CWO++ library," *Comput. Phys. Commun.* **183**, 1124–1138 (2012).
22. The computer physics communications program library CPC nonprofit use license agreement, <http://cpc.cs.qub.ac.uk/licence/licence.html>.
23. R. P. Muffoletto, J. M. Tyler, and J. E. Tohline, "Shifted Fresnel diffraction for computational holography," *Opt. Express* **15**, 5631–5640 (2007).
24. T. Colomb et al., "Numerical parametric lens for shifting, magnification, and complete aberration compensation in digital holographic microscopy," *J. Opt. Soc. Am. A* **23**, 3177–3190 (2006).
25. F. A. Jenkins and H. E. White, *Fundamentals of Optics*, McGraw-Hill Companies, New York (2001).
26. E. Román-Hernández et al., "Wavefronts and caustics of a spherical wave reflected by an arbitrary smooth surface," *J. Opt. Soc. Am. A* **26**, 2295–2305 (2009).
27. G. H. Yassen, J. A. Platt, and A. T. Hara, "Bovine teeth as substitute for human teeth in dental research: a review of literature," *J. Oral Sci.* **53**, 273–282 (2011).
28. N. Meredith et al., "Measurement of the microhardness and Young's modulus of human enamel and dentine using an indentation technique," *Archs. Oral Biol.* **41**, 539–545, (1996).
29. P. V. Soares et al., "Influence of restorative technique on the biomechanical behavior of endodontically treated maxillary premolars. Part II: strain measurement and stress distribution," *J. Prosthet. Dent.* **99**, 114–122 (2008).
30. T. Kreis, *Handbook of Holographic Interferometry: Optical and Digital Methods*, Wiley-VCH, Weinheim, Germany (2004).
31. D. Mas et al., "Fast numerical calculation of Fresnel patterns in convergent systems," *Opt. Commun.* **227**, 245–258 (2003).

Dejan V. Pantelić received his PhD degree in physics from the University of Belgrade, Serbia. He is a professor at the Photonics Center, Institute of Physics, University of Belgrade. His research interests include holography, microscopy, micro-optics, and biophotonics. He is a member of the Optical Society of America.

Dušan Ž. Grujić is a PhD student and research assistant at the Photonics Center, Institute of Physics, Belgrade, Serbia. He received his MSc degree at the Department of Applied Physics and Informatics, Faculty of Physics, University of Belgrade, Serbia. His research interests include application of digital holography techniques for measuring small changes in fluids and solid materials, direct laser writing, using parallel data processing in numerical simulations.

Darko M. Vasiljević received his PhD degree in mechanical engineering from the University of Belgrade, Serbia, in 1998. Since 2000, he has been a professor of optical instruments and optoelectronics in mechanical engineering at the University of Belgrade. Since 2005, he is a full-time researcher at the Institute of Physics, University of Belgrade. His research interests include optical design of complex optical and optoelectronic systems, microlenses, holography, and biophotonics.